Reversible Semiconducting-to-Metallic Phase Transition in Chemical Vapor Deposition Grown Monolayer WSe_2 and Applications for Devices

Yuqiang Ma, Bilu Liu,* Anyi Zhang, Liang Chen, Mohammad Fathi, Chenfei Shen, Ahmad N. Abbas, Mingyuan Ge, Matthew Mecklenburg, and Chongwu Zhou*

Department of Electrical Engineering, University of Southern California, Los Angeles, California 90089, United States

ABSTRACT Two-dimensional (2D) semiconducting monolayer transition metal dichalcogenides (TMDCs) have stimulated lots of interest because they are direct bandgap materials that have reasonably good mobility values. However, contact between most metals and semiconducting TMDCs like 2H phase WSe_2 are highly resistive, thus degrading the performance of field effect transistors (FETs) fabricated with WSe_2 as active channel materials. Recently, a phase engineering concept of 2D MoS_2 materials was developed, with improved device performance. Here, we applied this method to chemical vapor deposition (CVD) grown monolayer 2H-WSe_2 and demonstrated semiconducting-to-metallic phase transition in atomically thin WSe_2. We have also shown that metallic phase WSe_2 can be converted back to semiconducting phase, demonstrating the reversibility of this phase transition. In addition, we fabricated FETs based on these CVD-grown WSe_2 flakes with phase-engineered metallic 1T-WSe_2 as contact regions and intact semiconducting 2H-WSe_2 as active channel materials. The device performance is substantially improved with metallic phase source/drain electrodes, showing on/off current ratios of 10^7 and mobilities up to 66 $cm^2/V \cdot s$ for monolayer WSe_2. These results further suggest that phase engineering can be a generic strategy to improve device performance for many kinds of 2D TMDC materials.

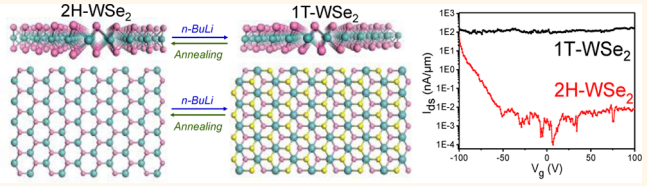

KEYWORDS: two-dimensional materials · transition metal dichalcogenides · tungsten diselenide · field effect transistor · contact · phase engineering · mobility

Monolayer transition metal dichalcogenides (TMDCs) with generalized formula of MX_2, where M is a transition metal (including groups 4 to 7 elements in the periodic table of elements) and X is a chalcogen (S, Se, or Te), have stimulated substantial interest in the past few years.[1−10] Recent studies on devices fabricated from either mechanically exfoliated or vapor-phase-grown TMDCs have revealed that they possess high current on/off ratios,[11,12] decent charge carrier mobilities,[1,13−18] subthreshold swings (SS) close to the theoretical limit,[15,19] reasonable energy storage capacity,[20] and interesting catalytic[21] and optical properties.[22−27] Among all TMDC materials, semiconducting 2H-MoS_2 is the one which has received most attention.[19,28−37] Meanwhile, there are also lots of recent papers studying electrical and mechanical properties of semiconducting 2H-WSe_2.[24−27,38−40] Compared to 2H-MoS_2, 2H-WSe_2 possesses a smaller bandgap (∼1.6 eV in monolayer WSe_2 and ∼1.8 eV in monolayer MoS_2) and it typically exhibits better electrical transport performance than MoS_2, in terms of charge carrier mobility.[3,41]

With a lattice structure similar to MoS_2, WSe_2 by its nature is a semiconductor with trigonal (2H) structure, where Se atoms locate in the lattice positions of a hexagonal close-packed structure. Planes of W atoms are sandwiched between two atomic layers of Se, such that each W is coordinated to six Se atoms in a trigonal prismatic geometry (2H). Another WSe_2 polytype, the octahedral coordination phase (1T), is based on tetragonal symmetry with one WSe_2 layer per repeating unit (schematic coordination of 2H and 1T-WSe_2 are shown in Figure 1a and 1b). As revealed by previous reports, chemical modification assisted in the phase transition between 2H and 1T phase TMDCs.[19,42,43] For example, by reacting with *n*-butyl lithium

* Address correspondence to chongwuz@usc.edu, biluliu@usc.edu.

Received for review April 21, 2015 and accepted June 28, 2015.

Published online June 30, 2015
10.1021/acsnano.5b02399

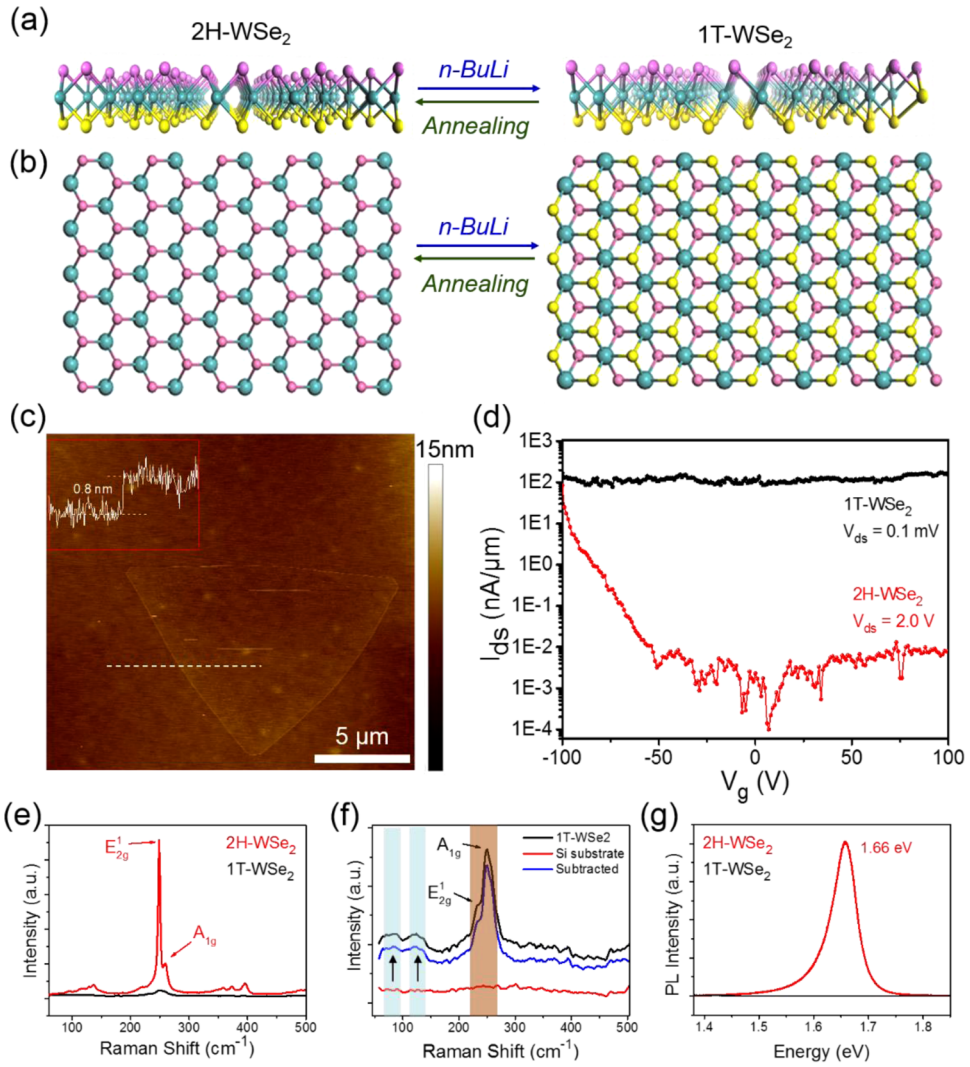

Figure 1. Atomic structures and reversible phase transitions between 2H and 1T phase WSe_2. (a) Side view of the 2H and 1T phase WSe_2. Pink atoms represent top layer selenium, cyan atoms represent tungsten, and yellow atoms represent bottom layer selenium. (b) Top view of 2H and 1T-WSe_2. Pink atoms represent top layer selenium, cyan atoms represent tungsten, and yellow atoms represent bottom layer selenium. (c) An AFM image along with a cross section height profile of a triangular WSe_2 flake. The height of this flake is ~0.8 nm, corresponding to a monolayer WSe_2. (d) FET device performance ($I_{ds}-V_g$ curves) comparison between 1T-WSe_2 and 2H-WSe_2. The 2H-WSe_2 device possesses an on/off ratio of 10^5, consistent with its semiconducting property. In contrast, 1T-WSe_2 FET shows little gate dependence, suggesting its metallic nature. (e) Raman spectra of 1T-WSe_2 and 2H-WSe_2 flakes. Typical Raman peaks of 2H-WSe_2 are observed while 1T-WSe_2 exhibits very weak signal. (f) Magnified Raman peaks of 1T-WSe_2. Black line is Raman signal for 1T-WSe_2 on Si/SiO_2 wafer. Blue line is Raman signal after substrate subtraction. Raman spectrum of 1T phase shows some new peaks at 50 and 150 cm^{-1} range (indicated by arrows). (g) PL spectra of 1T-WSe_2 and 2H-WSe_2 flakes. PL is significantly quenched in the 1T phase WSe_2.

(*n*-BuLi), Voiry *et al*. have systematically investigated the metallic phase contained in MoS_2, WS_2, and $MoSe_2$ nanosheets.[42] Moreover, Kappera *et al*. have recently reported that by using 1T-MoS_2 as source/drain contacts, the device performance of 2H-MoS_2 has been significantly improved compared with metal contacts.[19] However, in spite of the importance of WSe_2 in electronic and optical applications, the 2H-1T and 1T-2H phase transitions of WSe_2 were rarely reported. In addition, as for the stability of 1T-WSe_2, it is still an open yet important question.

For field effect transistors (FETs) with high performance, low contact resistance and ohmic behavior are crucial. In modern silicon electronics, good contact can be achieved by using highly doped source and drain contact regimes, on which metal pads can be deposited. There are several parameters that have impact on the device performance. For example, the lattice mismatch between metals and the channel materials may impair the efficiency of carrier injection. Work function of metals can also influence the efficiency of carrier injection, so that different metal contacts may lead to different device behaviors. Aiming at high-performance devices, FETs with mechanically exfoliated monolayer WSe_2 have been fabricated by Liu *et al*., using different kinds of metal contacts, and the devices with selected high work function metals showed small contact resistance and high drive current.[38]

Fang *et al.*, also reported p-type FETs based on exfoliated single-layer WSe_2 with chemically doped source/drain contacts using NO_2 and potassium, which exhibited high hole mobilities.[39] Nevertheless, even with the aforementioned achievements, the performance of WSe_2 FET may still be constrained by relatively high contact resistance, limited injection of carriers, and structural mismatch between the channel material and the electrodes.[19] In principle, 1T metallic phase WSe_2 could provide ideal contacts to 2H semiconducting WSe_2 and offer improved performance, but such studies have not been reported so far.

In this paper, we use chemical vapor deposition (CVD) synthesized 2H phase monolayer WSe_2, and report that *n*-BuLi treatment can convert 2H-WSe_2 into 1T-WSe_2. These two phases showed substantially different optical and electrical properties, as revealed by optical microscopy, Raman characterization, photoluminescence (PL) characterization, and electrical transport measurements. Importantly, by implementing the 1T phase as source and drain electrodes and intact CVD-grown 2H-WSe_2 as the channel material in FETs, we show that the effective mobility of these CVD-grown monolayer WSe_2 devices can reach up to 66 $cm^2/V \cdot s$, on/off ratio reaches 10^7, and the SS value is found to be 0.658 V/decade. These values are significantly better than those of devices with metal electrodes deposited directly on top of 2H phase WSe_2 in control experiments. More importantly, we found that by annealing in argon, we were able to convert 1T-WSe_2 back to 2H phase, demonstrating the reversibility of these phase transition processes. Taking recent reports on MoS_2 devices with phase-engineered contacts into account,[19] our results further suggest that phase engineering can be a generic approach to improve device performance of TMDC materials.

RESULTS AND DISCUSSIONS

Figure 1a and 1b show side view and top view schematics of the atomic structures of 2H and 1T WSe_2, and the proposed reversible phase transition in this study. The 2H-1T phase transition upon organolithium or organoalkali metal treatment has been well studied in some TMDCs, for example, MoS_2.[19,44] It has been proposed that when 2H phase MoS_2 is exposed to organolithium like *n*-BuLi, lithium will intercalate into the layers of MoS_2 and donate negative charges. To accommodate this additional negative charge, a local transformation of MoS_2 will occur, leading to a structural change of pristine 2H MoS_2 to 1T MoS_2.[19] The obtained metastable 1T MoS_2 is demonstrated to be negatively charged, and such negative charges help stabilizing 1T MoS_2, consistent with the above charge-donating picture. In a recent study, Wang *et al.* have proposed that for large alkali metals like sodium, the intercalation of sodium into the layers of 2H MoS_2 leads to a structure transformation to 1T MoS_2, since large alkali metal atoms like sodium will introduce large strain in the pristine lattice of 2H MoS_2, and lead to the formation of 1T MoS_2.[44] Considering the similarity between MoS_2 and WSe_2, it is reasonable to believe that they have very similar 2H to 1T conversion process, despite for the case of WSe_2, such a transformation has been rarely studied. In this study, the 2H-WSe_2 monolayer we used were grown *via* a CVD process. WO_3 and selenium powders were used as source materials for W and Se, and WSe_2 monolayers were directly grown on SiO_2/Si substrate at 950 °C (See Methods for details). To characterize the detailed structures of as-grown WSe_2 flakes, we performed systematical atomic force microscopy (AFM), Raman and PL studies. AFM characterization indicates that the thin flake shown in Figures 1c is a monolayer, as evident from the cross-sectional height profile in the inset of Figures 1c. The flake shows a triangular shape, which is in accordance with the trigonal prismatic Se−W−Se layers (space group $P6_3/mmc$).[45]

Starting from CVD-grown 2H-WSe_2 flakes, we can prepare 1T-WSe_2 samples *via* controlled treatment in *n*-BuLi. Specifically, 2H-WSe_2 samples were immersed into 5 mL of 1.6 M *n*-BuLi for 48 h. All the *n*-BuLi exposure was done in a glovebox filled with argon atmosphere at room temperature (Experimental details can be found in Methods). Based on the phase transition mechanism discussed above, the diffusion of lithium facilitates the structural transition, which is a quite slow thermodynamic process. We speculate that performing *n*-BuLi treatment at elevated temperatures, or exposing both faces of monolayer WSe_2 to *n*-BuLi solution, may accelerate the overall 2H-1T phase transition process. To compare the electrical properties of as-grown 2H-WSe_2 and *n*-BuLi treated WSe_2, we fabricated back-gated FETs using both intact 2H-WSe_2 and *n*-BuLi treated WSe_2 with e-beam lithography (EBL). Here we show a comparison of $I_{ds}-V_g$ curves for these WSe_2 devices (Figure 1d), where the device with *n*-BuLi treated WSe_2 as channel material showed little gate dependence and the untreated device (2H-WSe_2) exhibited an on/off ratio of 10^5. These results clearly demonstrate that the *n*-BuLi treated sample exhibit metallic behavior, while the intact 2H-WSe_2 exhibit p-type semiconducting behavior. Significantly, the bias voltage across the source and drain is 4 orders of magnitude smaller for *n*-BuLi treated WSe_2 than the untreated one (0.1 mV versus 2.0 V), revealing a greatly reduced resistance of WSe_2 after *n*-BuLi treatment. We note that FETs with *n*-BuLi treated WSe_2 showed resistances around 1 kΩ, which is much smaller than the reported resistance of 1T-MoS_2 device.[19] Considering this device as a monolayer resistor, the calculated sheet resistivity is found to be $\sim 10^{-6}$ $\Omega \cdot m$, which is 2 orders of magnitude larger than graphene, the material with lowest electrical resistivity.[46] These electrical measurements strongly suggest that *n*-BuLi

treatment has converted the original semiconducting 2H phase WSe_2 to metallic 1T phase.

In addition to their significant difference in electrical properties, the intact and *n*-BuLi treated WSe_2 show distinct optical properties, as revealed by Raman and PL measurements. Typical Raman spectra of 2H-WSe_2 and 1T-WSe_2 samples are shown in Figure 1e. 1T-WSe_2 showed extremely weak Raman and PL signals compared to 2H-WSe_2. This result can be understood since metals typically exhibit weak Raman signal, and cannot emit light. Similar phenomena were also observed in MoS_2 samples.[19,28] From the Raman spectrum of 2H-WSe_2, two strong characteristic peaks are observed in the region from 245 to 260 cm^{-1}, which can be assigned to E^1_{2g} (in-plane) and A_{1g} (out-of-plane) modes of 2H-WSe_2. The absence of the B^1_{2g} peak at ~304 cm^{-1} in Raman spectrum (which is a fingerprint of few layer WSe_2 and is absent in monolayer WSe_2) further confirms that the flakes are monolayer 2H-WSe_2, showing good consistency with AFM results. As for 1T phase WSe_2, the Raman signal is much weaker than 2H phase, hence the 1T phase Raman signal with 10 times magnification is shown in Figure 1f. As can be seen from the 1T-WSe_2 Raman spectrum, additional peaks are observed between 50 and 150 cm^{-1}. The Raman E^1_{2g} and A_{1g} peaks of 2H-WSe_2 are not completely disappeared, indicating that the converted material is not a pure 1T-WSe_2. Instead, it is a mixture of 1T and 2H-WSe_2, similar to the case of MoS_2.[19] Notably, for 1T-WSe_2 Raman spectrum, signal strength of E^1_{2g} peak from remaining 2H-WSe_2 is almost overwhelmed by signal strength of A_{1g} peak, while intact 2H-WSe_2 spectrum contrarily shows stronger E^1_{2g} peak than A_{1g}. Moreover, the PL spectra shown in Figure 1g further suggest that these two phases have substantial difference in band structures and optical properties. The PL spectrum for 2H-WSe_2 shows a sharp emission peak at ~1.66 eV, originating from the direct band gap monolayer WSe_2. For 1T-WSe_2, the PL signal is significantly quenched, which is consistent with the metallic property revealed in Figure 1d. We also used transmission electron microscopy (TEM) and fast Fourier transform (FFT) to characterize the structure of 2H and 1T-WSe_2 (Figure S1 in Supporting Information). Overall, our results are in agreement with a recent report, which has pointed out that 2H and 1T-MoS_2 share the same hexagonal diffraction pattern.[44] We also performed electron energy loss spectroscopy (EELS) studies to detect the amount of lithium residual in converted 1T WSe_2, since EELS is sensitive to light elements like lithium. The results show that the amount of lithium is below the detection limit, since no signal from lithium K-edge is observed (Figure S2 in Supporting Information).

To further illustrate the effect of *n*-BuLi treatment, we exposed select areas of 2H-WSe_2 to *n*-BuLi, thus aiming to transform these areas to 1T phase WSe_2. Patterning was first performed using EBL to expose certain regions of the WSe_2 flake for subsequent phase transition while protecting other regions unexposed with poly(methyl methacrylate) (PMMA). After the EBL writing and development, samples with selected exposure regions were immersed into 5 mL of 1.6 M *n*-BuLi for 48 h, so that WSe_2 in exposed regions were transformed into 1T phase while 2H-WSe_2 remained unchanged in regions protected by PMMA (Experimental details can be found in Methods). Figure 2a shows the schematic of patterning and *n*-BuLi treatment. With the patterning procedure described above, we fabricated a 2H-1T-2H-1T-2H laterally structured WSe_2 flake using

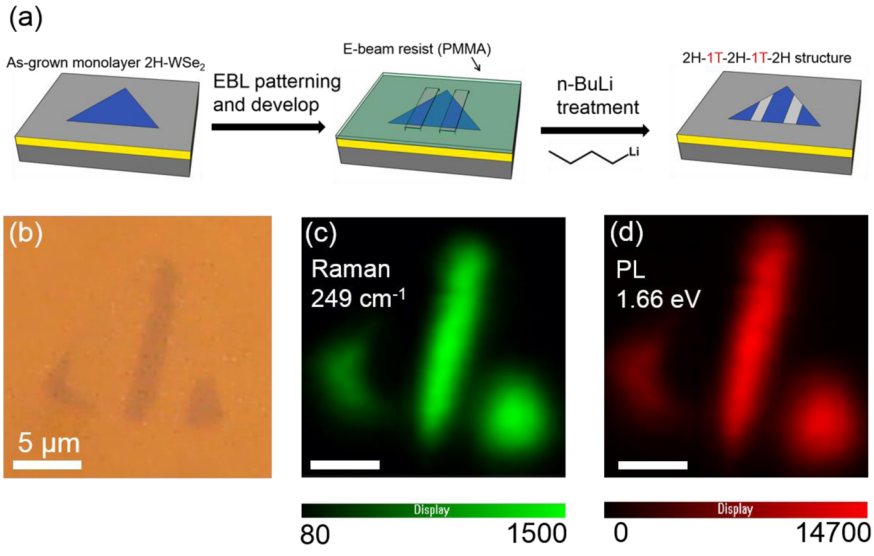

Figure 2. Characterization of a 2H-1T-2H-1T-2H laterally structured monolayer WSe_2 flake. (a) Schematic of lateral structure fabrication process. (b) Optical microscopy image of the WSe_2 flake after mask patterning and *n*-BuLi treatment, showing different contrast for treated (light regime) and untreated (dark regime) regimes. (c,d) Raman and PL intensity mapping of the same flake in panel b.

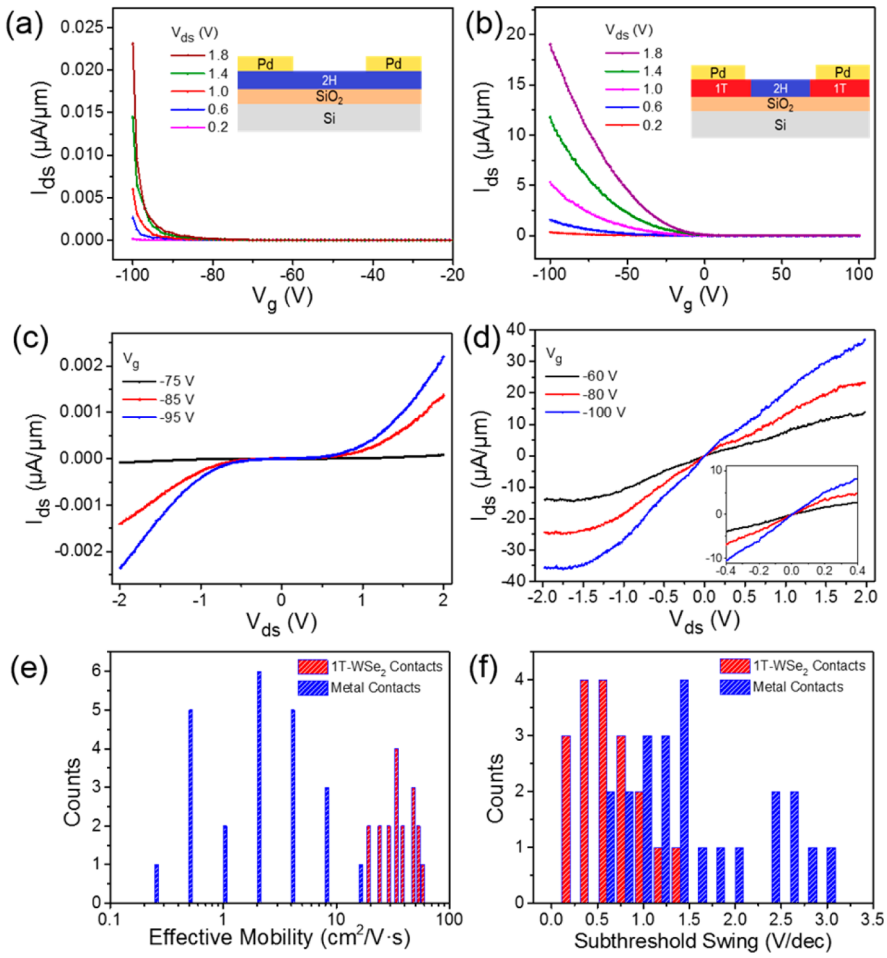

Figure 3. Device performance of monolayer WSe_2 flakes with metal contacts or 1T-WSe_2 contacts. (a) $I_{ds}-V_g$ curves for back-gated WSe_2 FET with metal contacts. Inset: Schematic image of the back-gated WSe_2 FET with metal contacts. (b) $I_{ds}-V_g$ curves for back-gated WSe_2 FET with 1T-WSe_2 as contacts. Inset: Schematic image of the back-gated WSe_2 FET with 1T-WSe_2 contacts. (c) $I_{ds}-V_{ds}$ curves for WSe_2 flakes with metal contacts. (d) $I_{ds}-V_{ds}$ curves for WSe_2 flakes with 1T-WSe_2 contacts. Inset in panel d: Magnified plot of panel d at a small bias. (e, f) Statistics about effective mobility (e) and SS (f) of 2H-WSe_2 FETs with metal contacts and 1T-WSe_2 contacts.

n-BuLi treatment, which was characterized by optical microscopy (Figure 2b), Raman mapping (Figure 2c), and PL mapping (Figure 2d). Interestingly, based on optical microscopy observations, we found that 1T and 2H phases WSe_2 possess distinct optical contrasts on silicon substrates with 285 nm SiO_2. Specifically, 1T phase WSe_2 is less visible than 2H-WSe_2. Thanks to this optical contrast between 1T-WSe_2 and 2H-WSe_2, optical microscopy could serve as a quick and nondestructive method to examine the phase transition process. Here, we also show Raman and PL intensity mapping on the same sample in Figure 2b. As can be clearly seen, the Raman and PL mapping duplicate the patterning of EBL and subsequent *n*-BuLi treatment, further confirming the success of selected-area phase transition of WSe_2. Also we have found that the *n*-BuLi diffused into the region underneath PMMA, especially for samples with long *n*-BuLi treatment time, so that some portions of the channel in the covered region have been converted into the 1T phase. Remarkable contrast differences between chemical-treated and untreated regions have also been observed under scanning electron microscopy (Figure S3 in Supporting Information), which reflects the difference in electrical conductivity.

One application of the selected-area 2H-1T conversion is to use metallic 1T-WSe_2 as contacts for 2H-WSe_2 FETs. To evaluate the effect of contacts on the performance of WSe_2 transistors, we have fabricated two types of back-gated FETs using CVD-grown WSe_2. In one type, we deposited Pd/Ti electrodes directly on top of as-grown 2H-WSe_2 (Figure 3a). In the other type, as-grown WSe_2 flakes were first converted into 1T-2H-1T lateral configurations using the selected-area *n*-BuLi treatment described previously, followed by Pd/Ti deposition on top of 1T phase regions (Figure 3b). Note that in both cases, the channel materials were the semiconducting 2H phase WSe_2, and the dielectric layer was 285 nm thick SiO_2. Figure 3 panels a and b are $I_{ds}-V_g$ curves for metal-contacted and 1T-WSe_2 contacted devices, respectively. Both of them show p-type behavior with high on/off ratios. However, as one can see, the normalized current is 3 orders of

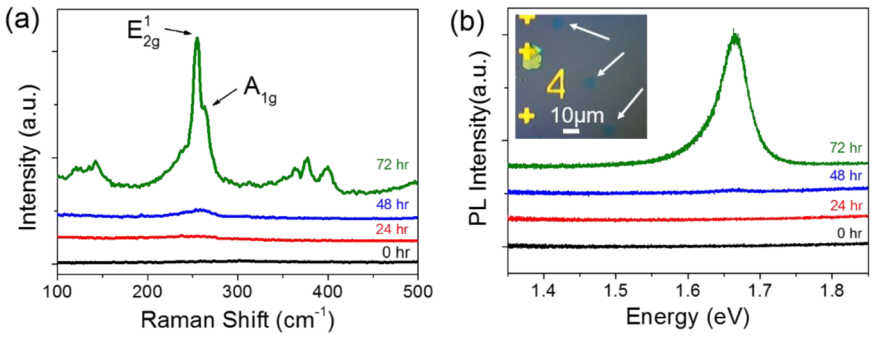

Figure 4. Reversibility of phase transition in monolayer 1T-WSe_2 and 2H-WSe_2 flakes. (a) Raman spectra evolution of 1T-WSe_2 at different annealing time. (b) PL spectra evolution of 1T-WSe_2 at different annealing time. Inset in panel b is an optical image of WSe_2 flakes after 72 h annealing in argon, showing structural integrity of these flakes after reversible phase transition.

magnitude larger in 1T-contacted devices than metal-contacted ones, suggesting a more effective carrier injection. The effective mobility of the 1T phase contacted WSe_2 devices is found to be ~66.68 $cm^2/(V \cdot s)$ in Figure 3b, while it is ~2 $cm^2/(V \cdot s)$ in Figure 3a. These effective mobility values are estimated using the standard FET model (see Methods for more details). We also compared the SS values of these two types of monolayer WSe_2 devices. The devices shown in Figure 3 panels a and b have SS values of 1.098 V/decade and 0.658 V/decade, respectively.

The $I_{ds}-V_{ds}$ family curves of the device with metal contacts on 2H-WSe_2 are shown in Figure 3c. A Schottky barrier can be clearly observed from the nonlinear $I_{ds}-V_{ds}$ curves, with a rather small normalized current of 25 nA/μm. In contrast, we observed a more ohmic contact behavior for devices with 1T phase WSe_2 as contacts, as shown in Figure 3d. The normalized current density for the 1T contact is around 20 μA/μm, which is 800 times larger than the devices using metal contacts. Very interestingly, *n*-BuLi treatment has shifted the threshold voltage of transistors from *ca.* −80 V to ~0 V, which may originate from the intrinsic negative charges in 1T phase WSe_2.[42]

In addition to a more ohmic contact behavior, we also observed current saturation behavior for 1T-WSe_2 contacted devices at $V_{ds} = -2$ V and $V_{ds} = +2$ V (Figure 3d), which showed a sharp difference with metal-contacted devices. We have fabricated multiple devices using these two kinds of contacts, and statistics of the key figures of merit from the two types of devices are shown in Figure 3e,f. Clearly, devices fabricated with 1T contacts showed significantly better performance than those devices using metal contacts, in terms of effective mobility and SS. These results suggest that charge injection into the channel is more efficient with 1T contacts than metal contacts. The lower SS values in the 1T-WSe_2 contacted devices could be accredited to lower density of interface traps.[28]

It is also worth noting that devices fabricated with 1T phase electrodes are highly reproducible, and the device performance is independent of the types of metal electrodes used. This phenomenon has also been observed by Kappera *et al.*[19] In our study, tens of devices with 1T-WSe_2 as contacts were fabricated, with different kinds of metal electrodes, and they show very similar behavior. For metal-contacted 2H-WSe_2 devices, the metal electrodes we have tried were 50 nm Au/1 nm Ti and 50 nm Pd/1 nm Ti, and these devices showed substantially worse performance than those with 1T contacts. Therefore, metallic 1T phase contacts are effective electrodes for high performance FETs made from CVD-grown WSe_2 monolayers.

Furthermore, we find that the phase transition process between 2H and 1T phase WSe_2 is reversible, which further offers chances for controlled property modification of WSe_2. With the help of Raman and PL measurements, we demonstrated that 1T phase WSe_2 flakes gradually converted back to 2H phase after long-time annealing treatment in a controlled argon environment. In an argon-filled glovebox, 1T phase WSe_2 was annealed at 180 °C to progressively restore the 2H phase, as supported by Raman and PL results (Figure 4a,b). From the Raman spectra, characteristic E^1_{2g} and A_{1g} peaks of 2H-WSe_2 can be observed and gradually dominate the spectra. Since this restoration process is quite slow (72 h), we may be able to quantitatively control the ratio of 2H phase and 1T phase by varying annealing time. Thus, it could be used as a convenient way to modify the properties of various TMDCs. Interestingly, we noticed that the restoration of 2H-WSe_2 from 1T-WSe_2 is not a linear process, that is, we observed little change within the first 48 h, and then a significantly accelerated restoration process between 48 and 72 h. We suspected that there might be a critical point for the 2H-WSe_2 restoration, like nucleation of 2H-WSe_2 small domains, which needs certain time to incubate. After reaching this critical point, further restoration could be significantly faster. Further studies are needed to study the details of these phase transition processes. In addition to the sample heated up to 180 °C, a controlled experiment was also performed in the same argon environment without annealing, that is, the sample was kept in an argon environment at room

temperature. Our Raman and PL results show that the control samples are quite stable (Figure S4 in Supporting Information). We also noted that in addition to heating in argon, exposure to light and air could also convert the 1T phase WSe_2 to 2H phase. This result is in agreement with previous reports on 1T-MoS_2, which pointed out that 1T-MoS_2 is thermally unstable and any characterization of this material must take into account the thermal history of each sample.[42,47]

CONCLUSION

We have demonstrated the feasibility to locally pattern and convert CVD-grown monolayer semiconducting 2H WSe_2 to metallic 1T phase WSe_2 *via* controlled *n*-BuLi treatment. We showed that the two phases have distinct optical and electrical properties. More importantly, metallic 1T phase WSe_2 was demonstrated to be an effective electrode for high performance FETs for 2H-WSe_2 monolayers. FETs with 1T phase contacts demonstrated higher effective mobilities (up to 66 $cm^2/(V\cdot s)$), high on/off ratios (up to 10^7), and better SS values (0.658 V/decade) than devices with metal contacts like Pd/Ti and Au/Ti. Also we showed that the transition from 1T phase WSe_2 to 2H phase WSe_2 is reversible, which can be further used for controlled property modification of WSe_2 and other TMDCs. These results further suggest phase engineering could be a general approach to modify properties for various TMDCs.

METHODS

CVD Growth of WSe_2 Flakes. Details of CVD growth of WSe_2 flakes were reported in our recent paper.[48] In brief, a three zone furnace is used for CVD growth of WSe_2. In a typical experiment, selenium powder (440 mg) was put in the first zone, and WO_3 powder (260 mg) was put in the third zone. The distance between the two sources was 55 cm. The temperatures of WO_3 and Se were 950 and 540 °C, respectively. Silicon wafers with 285 nm SiO_2 layer were used as growth substrates. WSe_2 growth was conducted at ambient pressure under an Ar/H_2 flow rate of 320/20 sccm for 15 min.

Reversible 2H-1T WSe_2 Phase Transition. The as-grown 2H phase WSe_2 was converted into 1T phase *via* *n*-BuLi treatment. Specifically, the 2H-WSe_2 sample was immersed in 5 mL of 1.6 M *n*-butyl lithium (Sigma-Aldrich) for 48 h in an argon-filled glovebox (Unilab, Mbraun, Germany, with water and O_2 concentrations less than 0.1 ppm). After reaction, the sample was thoroughly washed with hexane in the glovebox. For the reverse transition, that is, 1T to 2H transition, the 1T-WSe_2 was placed on the hot plate at 180 °C in the glovebox for different durations. As control experiments, 1T-WSe_2 was put in a glovebox at room temperature, and the 1T to 2H phase transition was not observed.

Characterization. The as-grown WSe_2 flakes were characterized by optical microscopy, Raman spectroscopy (532 nm laser, Renishaw Raman), AFM (DI 3100 Digital Instruments), TEM (JEOL 2100F, 200 kV), and field emission scanning electron microscope (Zeiss Supra 35 VP at an electron accelerating voltage of 5 kV). For TEM and EELS characterization, the CVD-grown 2H-WSe_2 flakes were transferred onto TEM grid using a PMMA-medicated method.[49]

WSe_2 Device Fabrication and Measurements. The 2H phase back-gated WSe_2 transistors were directly fabricated on Si/SiO_2 substrates on which WSe_2 flakes were grown, using EBL. A bilayer PMMA was first spin-coated onto the Si/SiO_2 surface. Then, EBL was conducted to pattern source/drain electrodes, followed by development, metal deposition, and lift-off processes. Pd/Ti electrodes (50 nm/1 nm) were deposited at 1×10^{-6} Torr using an e-beam evaporator. The device measurements were performed using Aglient 4156B in ambient condition.

For 1T-2H-1T laterally structured WSe_2 devices, alignment markers and electrodes were fabricated using EBL. The 1T regime of the phase engineered device was obtained *via* *n*-BuLi treatment as described above.

The effective mobility is calculated with the following equation:[50]

$$\mu = \frac{L}{W}\frac{1}{C_{ox}V_{ds}}\frac{dI_{ds}}{dV_g}$$

where L and W are the channel length and width of the device, V_{ds} is the source and drain voltage, I_{ds} is the current flowing from source to drain, and V_g is the gate voltage. C_{ox} is the gate capacitance per unit area.

Conflict of Interest: The authors declare no competing financial interest.

Acknowledgment. This work was financially supported by the Air Force Office of Scientific Research (AFOSR), and King Abdulaziz City for Science and Technology (KACST). TEM data presented in this article were acquired at the Center for Electron Microscopy and Microanalysis at the University of Southern California. We acknowledge Stephen Cronin of University of Southern California for access to Raman facility. We also acknowledge Adam Stieg of University of California, Los Angeles for access to AFM facility.

Supporting Information Available: Additional SEM, TEM, PL, and Raman results. The Supporting Information is available free of charge on the ACS Publications website at DOI: 10.1021/acsnano.5b02399.

REFERENCES AND NOTES

1. Chhowalla, M.; Shin, H. S.; Eda, G.; Li, L. J.; Loh, K. P.; Zhang, H. The Chemistry of Two-Dimensional Layered Transition Metal Dichalcogenide Nanosheets. *Nat. Chem.* **2013**, *5*, 263–275. DOI: 10.1038/nchem.1589.
2. Geim, A. K.; Grigorieva, I. V. Van Der Waals Heterostructures. *Nature* **2013**, *499*, 419–425. DOI: 10.1038/nature12385.
3. Wang, Q. H.; Kalantar-Zadeh, K.; Kis, A.; Coleman, J. N.; Strano, M. S. Electronics and Optoelectronics of Two-Dimensional Transition Metal Dichalcogenides. *Nat. Nanotechnol.* **2012**, *7*, 699–712. DOI: 10.1038/nnano.2012.193.
4. Yoffe, A. D. Electronic Properties of Some Chain and Layer Compounds. *Chem. Soc. Rev.* **1976**, *5*, 51–78. DOI: 10.1039/cs9760500051.
5. Liu, B. L.; Chen, L.; Liu, G.; Abbas, A. N.; Fathi, M.; Zhou, C. W. High-Performance Chemical Sensing Using Schottky-Contacted Chemical Vapor Deposition Grown Mono Layer MoS_2 Transistors. *ACS Nano* **2014**, *8*, 5304–5314. DOI: 10.1021/nn5015215.
6. Hersam, M. C.; LeRoy, B. J. Preface to Special Topic: Two-Dimensional Materials. *APL Mater.* **2014**, *2*, 092201. DOI: 10.1063/1.4893496.
7. Gong, Y. J.; Lin, J. H.; Wang, X. L.; Shi, G.; Lei, S. D.; Lin, Z.; Zou, X. L.; Ye, G. L.; Vajtai, R.; Yakobson, B. I.; et al. Vertical and in-Plane Heterostructures from WS_2/MoS_2 Monolayers. *Nat. Mater.* **2014**, *13*, 1135–1142. DOI: 10.1038/nmat4091.
8. Roy, T.; Tosun, M.; Cao, X.; Fang, H.; Lien, D. H.; Zhao, P. D.; Chen, Y. Z.; Chueh, Y. L.; Guo, J.; Javey, A. Dual-Gated MoS_2/WSe_2 Van Der Waals Tunnel Diodes and Transistors. *ACS Nano* **2015**, *9*, 2071–2079. DOI: 10.1021/nn507278b.
9. Huang, S. X.; Ling, X.; Liang, L. B.; Kong, J.; Terrones, H.; Meunier, V.; Dresselhaus, M. S. Probing the Interlayer Coupling of Twisted Bilayer MoS_2 Using Photoluminescence

Spectroscopy. *Nano Lett.* **2014**, *14*, 5500–5508. DOI: 10.1021/nl5014597.
10. Sie, E. J.; McIver, J.; Lee, Y. H.; Fu, L.; Kong, J.; Gedik, N. Valley-Selective Optical Stark Effect in Monolayer WS_2. *Nat. Mater.* **2014**, *14*, 290–294. DOI: 10.1038/nmat4156.
11. Zhao, P. D.; Kiriya, D.; Azcatl, A.; Zhang, C. X.; Tosun, M.; Liu, Y. S.; Hettick, M.; Kang, J. S.; McDonnell, S.; Santosh, K. C.; et al. Air Stable p-Doping of WSe_2 by Covalent Functionalization. *ACS Nano* **2014**, *8*, 10808–10814. DOI: 10.1021/nn5047844.
12. Kiriya, D.; Tosun, M.; Zhao, P. D.; Kang, J. S.; Javey, A. Air-Stable Surface Charge Transfer Doping of MoS_2 by Benzyl Viologen. *J. Am. Chem. Soc.* **2014**, *136*, 7853–7856. DOI: 10.1021/ja5033327.
13. Pu, J.; Yomogida, Y.; Liu, K. K.; Li, L. J.; Iwasa, Y.; Takenobu, T. Highly Flexible MoS_2 Thin-Film Transistors with Ion Gel Dielectrics. *Nano Lett.* **2012**, *12*, 4013–4017. DOI: 10.1021/nl301335q.
14. Chang, H. Y.; Yang, S. X.; Lee, J. H.; Tao, L.; Hwang, W. S.; Jena, D.; Lu, N. S.; Akinwande, D. High-Performance, Highly Bendable MoS_2 Transistors with High-K Dielectrics for Flexible Low-Power Systems. *ACS Nano* **2013**, *7*, 5446–5452. DOI: 10.1021/nn401429w.
15. Zhou, H.; Wang, C.; Shaw, J. C.; Cheng, R.; Chen, Y.; Huang, X.; Liu, Y.; Weiss, N. O.; Lin, Z.; Huang, Y.; et al. Large Area Growth and Electrical Properties of P-Type WSe_2 Atomic Layers. *Nano Lett.* **2014**, *15*, 709–713. DOI: 10.1021/nl504256y.
16. Tosun, M.; Chuang, S.; Fang, H.; Sachid, A. B.; Hettick, M.; Lin, Y. J.; Zeng, Y. P.; Javey, A. High-Gain Inverters Based on WSe_2 Complementary Field-Effect Transistors. *ACS Nano* **2014**, *8*, 4948–4953. DOI: 10.1021/nn5009929.
17. Wang, H.; Yu, L. L.; Lee, Y. H.; Shi, Y. M.; Hsu, A.; Chin, M. L.; Li, L. J.; Dubey, M.; Kong, J.; Palacios, T. Integrated Circuits Based on Bilayer MoS_2 Transistors. *Nano Lett.* **2012**, *12*, 4674–4680. DOI: 10.1021/nl302015v.
18. Chen, L.; Liu, B. L.; Abbas, A. N.; Ma, Y. Q.; Fang, X.; Liu, Y. H.; Zhou, C. W. Screw-Dislocation-Driven Growth of Two-Dimensional Few-Layer and Pyramid-Like WSe_2 by Sulfur-Assisted Chemical Vapor Deposition. *ACS Nano* **2014**, *8*, 11543–11551. DOI: 10.1021/nn504775f.
19. Kappera, R.; Voiry, D.; Yalcin, S. E.; Branch, B.; Gupta, G.; Mohite, A. D.; Chhowalla, M. Phase-Engineered Low-Resistance Contacts for Ultrathin MoS_2 Transistors. *Nat. Mater.* **2014**, *13*, 1128. DOI: 10.1038/nmat4080.
20. Chang, K.; Chen, W. X. L-Cysteine-Assisted Synthesis of Layered MoS_2/Graphene Composites with Excellent Electrochemical Performances for Lithium Ion Batteries. *ACS Nano* **2011**, *5*, 4720–4728. DOI: 10.1021/nn200659w.
21. Hinnemann, B.; Moses, P. G.; Bonde, J.; Jorgensen, K. P.; Nielsen, J. H.; Horch, S.; Chorkendorff, I.; Norskov, J. K. Biornimetic Hydrogen Evolution: MoS_2 Nanoparticles as Catalyst for Hydrogen Evolution. *J. Am. Chem. Soc.* **2005**, *127*, 5308–5309. DOI: 10.1021/ja0504690.
22. Groenendijk, D. J.; Buscema, M.; Steele, G. A.; de Vasconcellos, S. M.; Bratschitsch, R.; van der Zant, H. S. J.; Castellanos-Gomez, A. Photovoltaic and Photothermoelectric Effect in a Double-Gated WSe_2 Device. *Nano Lett.* **2014**, *14*, 5846–5852. DOI: 10.1021/nl502741k.
23. Lopez-Sanchez, O.; Lembke, D.; Kayci, M.; Radenovic, A.; Kis, A. Ultrasensitive Photodetectors Based on Monolayer MoS_2. *Nat. Nanotechnol.* **2013**, *8*, 497–501. DOI: 10.1038/nnano.2013.100.
24. Ross, J. S.; Klement, P.; Jones, A. M.; Ghimire, N. J.; Yan, J. Q.; Mandrus, D. G.; Taniguchi, T.; Watanabe, K.; Kitamura, K.; Yao, W.; et al. Electrically Tunable Excitonic Light-Emitting Diodes Based on Monolayer WSe_2 p-n Junctions. *Nat. Nanotechnol.* **2014**, *9*, 268–272. DOI: 10.1038/nnano.2014.26.
25. Pospischil, A.; Furchi, M. M.; Mueller, T. Solar-Energy Conversion and Light Emission in an Atomic Monolayer P-N Diode. *Nat. Nanotechnol.* **2014**, *9*, 257–261. DOI: 10.1038/nnano.2014.14.
26. Baugher, B. W. H.; Churchill, H. O. H.; Yang, Y. F.; Jarillo-Herrero, P. Optoelectronic Devices Based on Electrically Tunable p-n Diodes in a Monolayer Dichalcogenide. *Nat. Nanotechnol.* **2014**, *9*, 262–267. DOI: 10.1038/nnano.2014.25.
27. Desai, S. B.; Seol, G.; Kang, J. S.; Fang, H.; Battaglia, C.; Kapadia, R.; Ager, J. W.; Guo, J.; Javey, A. Strain-Induced Indirect to Direct Bandgap Transition in Multi Layer WSe_2. *Nano Lett.* **2014**, *14*, 4592–4597. DOI: 10.1021/nl501638a.
28. Kappera, R.; Voiry, D.; Yalcin, S. E.; Jen, W.; Acerce, M.; Torrel, S.; Branch, B.; Lei, S. D.; Chen, W. B.; Najmaei, S.; et al. Metallic 1T Phase Source/Drain Electrodes for Field Effect Transistors from Chemical Vapor Deposited MoS_2. *APL Mater.* **2014**, *2*, 092516. DOI: 10.1063/1.4896077.
29. Radisavljevic, B.; Radenovic, A.; Brivio, J.; Giacometti, V.; Kis, A. Single-Layer MoS_2 Transistors. *Nat. Nanotechnol.* **2011**, *6*, 147–150. DOI: 10.1038/nnano.2010.279.
30. Jariwala, D.; Sangwan, V. K.; Late, D. J.; Johns, J. E.; Dravid, V. P.; Marks, T. J.; Lauhon, L. J.; Hersam, M. C. Band-Like Transport in High Mobility Unencapsulated Single-Layer MoS_2 Transistors. *Appl. Phys. Lett.* **2013**, *102*, 173107. DOI: 10.1063/1.4803920.
31. Ji, Q. Q.; Zhang, Y. F.; Gao, T.; Zhang, Y.; Ma, D. L.; Liu, M. X.; Chen, Y. B.; Qiao, X. F.; Tan, P. H.; Kan, M.; et al. Epitaxial Monolayer MoS_2 on Mica with Novel Photoluminescence. *Nano Lett.* **2013**, *13*, 3870–3877. DOI: 10.1021/nl401938t.
32. Ling, X.; Lee, Y. H.; Lin, Y. X.; Fang, W. J.; Yu, L. L.; Dresselhaus, M. S.; Kong, J. Role of the Seeding Promoter in MoS_2 Growth by Chemical Vapor Deposition. *Nano Lett.* **2014**, *14*, 464–472. DOI: 10.1021/nl4033704.
33. Zhang, L. M.; Liu, K. H.; Wong, A. B.; Kim, J.; Hong, X. P.; Liu, C.; Cao, T.; Louie, S. G.; Wang, F.; Yang, P. D. Three-Dimensional Spirals of Atomic Layered MoS_2. *Nano Lett.* **2014**, *14*, 6418–6423. DOI: 10.1021/nl502961e.
34. Lui, C. H.; Frenzel, A. J.; Pilon, D. V.; Lee, Y. H.; Ling, X.; Akselrod, G. M.; Kong, J.; Gedik, N. Trion-Induced Negative Photoconductivity in Monolayer MoS_2. *Phys. Rev. Lett.* **2014**, *113*, 166801. DOI: 10.1103/PhysRevLett.113.166801.
35. Balendhran, S.; Walia, S.; Nili, H.; Ou, J. Z.; Zhuiykov, S.; Kaner, R. B.; Sriram, S.; Bhaskaran, M.; Kalantar-zadeh, K. Two-Dimensional Molybdenum Trioxide and Dichalcogenides. *Adv. Funct. Mater.* **2013**, *23*, 3952–3970. DOI: 10.1002/adfm.201300125.
36. Gong, Y. J.; Liu, Z.; Lupini, A. R.; Shi, G.; Lin, J. H.; Najmaei, S.; Lin, Z.; Elias, A. L.; Berkdemir, A.; You, G.; et al. Band Gap Engineering and Layer-by-Layer Mapping of Selenium-Doped Molybdenum Disulfide. *Nano Lett.* **2014**, *14*, 442–449. DOI: 10.1021/nl4032296.
37. Jariwala, D.; Sangwan, V. K.; Wu, C. C.; Prabhumirashi, P. L.; Geier, M. L.; Marks, T. J.; Lauhon, L. J.; Hersam, M. C. Gate-Tunable Carbon Nanotube-MoS_2 Heterojunction p-n Diode. *Proc. Natl. Acad. Sci. U. S. A.* **2013**, *110*, 18076–18080. DOI: 10.1073/pnas.1317226110.
38. Liu, W.; Kang, J. H.; Sarkar, D.; Khatami, Y.; Jena, D.; Banerjee, K. Role of Metal Contacts in Designing High-Performance Monolayer n-Type WSe_2 Field Effect Transistors. *Nano Lett.* **2013**, *13*, 1983–1990. DOI: 10.1021/nl304777e.
39. Fang, H.; Chuang, S.; Chang, T. C.; Takei, K.; Takahashi, T.; Javey, A. High-Performance Single Layered WSe_2 p-FETs with Chemically Doped Contacts. *Nano Lett.* **2012**, *12*, 3788–3792. DOI: 10.1021/nl301702r.
40. Chen, K.; Kiriya, D.; Hettick, M.; Tosun, M.; Ha, T. J.; Madhvapathy, S. R.; Desai, S.; Sachid, A.; Javey, A. Air Stable n-Doping of WSe_2 by Silicon Nitride Thin Films with Tunable Fixed Charge Density. *APL Mater.* **2014**, *2*, 092504. DOI: 10.1063/1.4891824.
41. Chuang, H. J.; Tan, X. B.; Ghimire, N. J.; Perera, M. M.; Chamlagain, B.; Cheng, M. M. C.; Yan, J. Q.; Mandrus, D.; Tomanek, D.; Zhou, Z. X. High Mobility WSe_2 P- and n-Type Field-Effect Transistors Contacted by Highly Doped Graphene for Low-Resistance Contacts. *Nano Lett.* **2014**, *14*, 3594–3601. DOI: 10.1021/nl501275p.
42. Voiry, D.; Goswami, A.; Kappera, R.; Silva, C. D. C. E.; Kaplan, D.; Fujita, T.; Chen, M. W.; Asefa, T.; Chhowalla, M. Covalent Functionalization of Monolayered Transition Metal Dichalcogenides by Phase Engineering. *Nat. Chem.* **2014**, *7*, 45–49. DOI: 10.1038/nchem.2108.

43. Ambrosi, A.; Sofer, Z.; Pumera, M. 2H --> 1T Phase Transition and Hydrogen Evolution Activity of MoS_2, $MoSe_2$, WS_2 and WSe_2 Strongly Depends on the MX Composition. *Chem. Commun.* **2015**, *51*, 8450. DOI: 10.1039/C5CC00803D.
44. Wang, X. F.; Shen, X.; Wang, Z. X.; Yu, R. C.; Chen, L. Q. Atomic-Scale Clarification of Structural Transition of MoS_2 Upon Sodium Intercalation. *ACS Nano* **2014**, *8*, 11394–11400. DOI: 10.1021/nn505501v.
45. Coehoorn, R.; Haas, C.; Dijkstra, J.; Flipse, C. J. F.; Degroot, R. A.; Wold, A. Electronic-Structure of $MoSe_2$, MoS_2, and WSe_2 0.1. Band-Structure Calculations and Photoelectron-Spectroscopy. *Phys. Rev. B: Condens. Matter Mater. Phys.* **1987**, *35*, 6195–6202. DOI: 10.1103/PhysRevB.35.6195.
46. Schwierz, F. Graphene Transistors. *Nat. Nanotechnol.* **2010**, *5*, 487–496. DOI: 10.1038/nnano.2010.89.
47. Dungey, K. E.; Curtis, M. D.; Penner-Hahn, J. E. Structural Characterization and Thermal Stability of MoS_2 Intercalation Compounds. *Chem. Mater.* **1998**, *10*, 2152–2161. DOI: 10.1021/cm980034u.
48. Liu, B. L.; Fathi, M. A.; Chen, L.; Abbas, A. N.; Ma, Y. Q.; Zhou, C. W. Chemical Vapor Deposition Growth of Monolayer WSe_2 with Tunable Device Characteristics and Growth Mechanism Study. *ACS Nano* **2015**, *9*, 6119–6127. DOI: 10.1021/acsnano.5b01301.
49. Liu, B. L.; Ren, W. C.; Gao, L. B.; Li, S. S.; Pei, S. F.; Liu, C.; Jiang, C. B.; Cheng, H. M. Metal-Catalyst-Free Growth of Single-Walled Carbon Nanotubes. *J. Am. Chem. Soc.* **2009**, *131*, 2082–2083. DOI: 10.1021/ja8093907.
50. Stassen, A. F.; de Boer, R. W. I.; Iosad, N. N.; Morpurgo, A. F. Influence of the Gate Dielectric on the Mobility of Rubrene Single-Crystal Field-Effect Transistors. *Appl. Phys. Lett.* **2004**, *85*, 3899–3901. DOI: 10.1063/1.1812368.